IEEE Access
Multidisciplinary ⋮ Rapid Review ⋮ Open Access Journal

Received August 27, 2020, accepted September 8, 2020, date of publication September 14, 2020, date of current version September 24, 2020.

Digital Object Identifier 10.1109/ACCESS.2020.3023649

Study on Wind Energy Harvesting Effect of a Vehicle-Mounted Piezo-Electromagnetic Hybrid Energy Harvester

XIA LI, ZHIYUAN LI, CHENG BI, BENXUE LIU, AND YUFENG SU, (Member, IEEE)
School of Mechanical and Power Engineering, Zhengzhou University, Zhengzhou 450001, China

Corresponding authors: Xia Li (jennyhit@163.com) and Benxue Liu (liubenxue@zzu.edu.cn)

This work was supported by the National Natural Science Foundation of China under Grant U1904169 and Grant 51107121.

ABSTRACT To realize the self-power of the vehicle micro-sensors, a piezo-electromagnetic hybrid vehicle-mounted energy harvester is proposed to recover the wind and vibration energy generated during driving. This energy harvester includes a flutter piezoelectric energy harvesting structure (FPEH) and an electromagnetic vibration energy harvester structure (EVEH). The combination of the two structures can improve the energy harvesting effect and reduce the cut-in wind speed. The coupled vibration mathematical model is established to predict the output performance of the wind energy harvesting effect. The effects of the different distances between magnets on the output are discussed. And the vibration characteristics of piezoelectric and electromagnetic vibrators are analyzed. Results show that the energy-harvesting effect is the best when the distance between magnets is 30mm. At the same time, the numerical simulation proves that the wind energy harvesting effect of the hybrid structure is better than the classic flutter structure. The experimental verification is carried out, and the experimental results are consistent with the theoretical prediction results, which verified the correctness of the theory. The optimal load of FPEH is 70kΩ, and the optimal load of EVEH is 60Ω. Under these conditions, when the wind speed is 18m/s, the peak output power of FPEH is 14.5mW, and that of EVEH is 31.8mW.

INDEX TERMS Flutter, piezo-electromagnetic hybrid, vehicle-mounted, wind energy harvester.

I. INTRODUCTION

Traveling on roads, vehicles will inevitably generate a lot of recyclable energy [1], [2], and cars are equipped with many low-power microelectronic devices and wireless sensors [3], [4], which provides an application foundation for applying micro energy harvesters to cars. There are several forms of recyclable energy generated during driving, such as vibration energy, wind energy, heat energy, and even solar energy [5], [6]. Among them, vibration energy and wind energy have the characteristics of high recyclability and convenient recovery during driving [4]. A micro harvester that recovers vibration energy and wind energy at the same time can replace traditional chemical batteries to supply power for microsensors or wireless electronic devices. And it can effectively solve the problems of battery replacement, environmental pollution, and high cost [7]–[10].

Due to the obvious advantages of high power density and no electromagnetic interference, the piezoelectric aeroelastic energy harvesting has become a promising research topic of the global research teams in recent decades [11]–[14]. The aeroelastic piezoelectric energy harvesters mainly include galloping [15]–[17], flutter [18]–[21], vortex-induced [22]–[24], and wake-induced vibration [25], [26] energy harvesters. Among them, vortex-induced vibration and wake-induced vibration piezoelectric energy harvesters mainly capture energy for low-speed fluids. Flutter and gallop piezoelectric energy harvesters have the characteristics of self-excitation, divergence, nonlinearity, large amplitude, and large deformation, and are more suitable for energy capture of high-speed fluids [27]. Flutter piezoelectric energy harvesters can obtain persistent oscillations of acceptable amplitude over a wide range of resonance wind speed [28]. Bryant and Garcia [18] originally proposed a flutter-based aeroelastic energy harvester (FAEH), and they found that the harvester oscillated in a limit cycle at higher wind speeds above a critical wind speed. Abdelkefi *et al.* [19] investigated the influence of structural and aerodynamic nonlinearities on the dynamic behavior of a FAEH system, and they found that the variations in the torsional spring has the most influence

The associate editor coordinating the review of this manuscript and approving it for publication was Muhammad Maaz Rehan.

This work is licensed under a Creative Commons Attribution 4.0 License. For more information, see https://creativecommons.org/licenses/by/4.0/

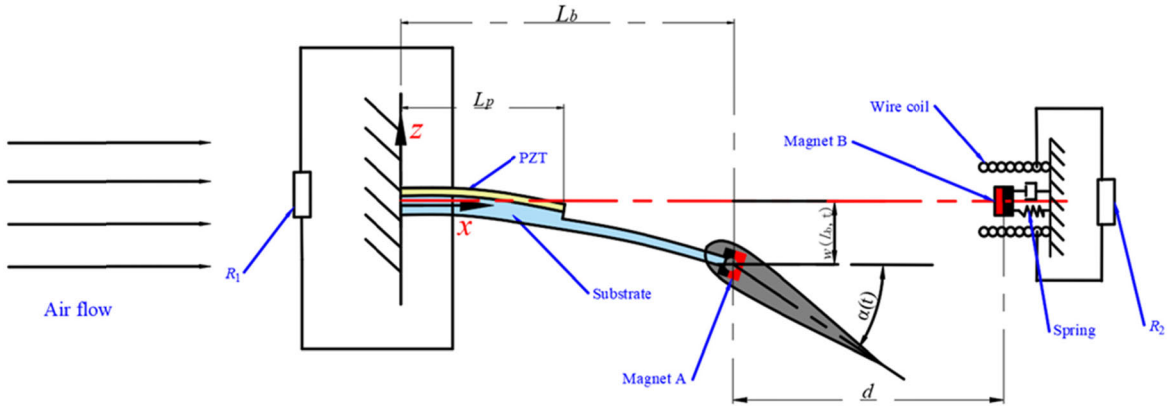

FIGURE 1. Structural schematic of the hybrid vehicle-mounted energy harvester.

and could change the system's instability to the subcritical type. Wu *et al.* [29] proposed a piezo-aeroelastic energy harvester based on an airfoil with double plunge degrees of freedom. It is numerically demonstrated that the double-plunge energy harvester outperforms its equivalent counterpart using the pitch–plunge configuration in terms of both the average power output and energy harvesting efficiency as the flow velocity exceeds the cut-in speed. Li *et al.* [30], [31] designed magnetically coupled nonlinear flutter wind energy harvesters, and the experimental and numerical results confirmed that the nonlinear harvesters have lower cut-in wind speed and higher voltage output under low wind speed.

As the electromagnetic suspension energy recovery system has the characteristics of high recovery efficiency, fast response, and strong controllability, the research of vehicle vibration energy collection mainly focuses on the recovery of vibration energy of vehicle suspensions [32], [33]. However, this kind of energy harvesters need to change the internal structure of suspensions, and the cost is relatively high, thus they are not suitable for the power supply of the low-power microelectronic system. In addition, the tire-embedded piezoelectric energy harvesters are also common designs [34]. For example, Sadeqi *et al.* [35] designed a broadband piezoelectric energy harvester for rotary motion applications by introducing a coupled spring-mass to the PZT beam undergoing rotary motion. Khameneifar *et al.* [36] convert mechanical strain into electricity through PZT stacks inside the tire, to provide power for the wireless sensors inside the tire. The analytical model calculated that 14 stacks of piezoelectric devices would harvest about 42 mW of power. Because the embedded tire structure is not easy to install and the size requirements are more stringent, it does not have good applicability.

Changing a single beam piezoelectric energy harvester to a piezo-electromagnetic hybrid system is often considered an effective method of frequency extension and output performance improving [37]–[39]. Xu *et al.* [40] designed a piezoelectric-electromagnetic hybrid vibration energy harvester which has two peak powers and it is 2.36 times more than the combined output power of the linear piezoelectric energy harvester and linear electromagnetic energy harvester at 22.6 Hz. Tadesse *et al.* [41] reported a hybrid energy harvester (HEH) using piezoelectric and electromagnetic mechanisms. It consisted of a piezoelectric cantilever beam and a permanent magnet attached at the tip of a spring, which oscillated within a stationary coil. In addition, Li *et al.* [42] conducted a theoretical and experimental analysis of piezoelectric-electromagnetic energy harvester under random vibration, and found that the maximum average output power is related to the vibration frequency and acceleration. The combination of piezoelectric and electromagnetic energy harvesting structures will effectively improve the energy harvesting effect.

This article aims to design a piezo-electromagnetic hybrid vehicle-mounted energy harvester. This harvester is mainly composed of a flutter piezoelectric energy harvester (FPEH) and an electromagnetic vibration energy harvester (EVEH). The two harvesters are coupled with each other by the end magnetic force. The harvester can recover wind energy when the road surface is relatively flat and wind speed is high, and recover vibration energy when the road condition is poor. This paper mainly establishes the coupling mathematical model of the wind energy harvesting effect of the hybrid structure. By numerical simulation, the output characteristics are predicted and analyzed. By conducting energy harvesting experiments, the correctness of the mathematical model is verified.

II. STRUCTURE AND WORKING PRINCIPLE

As shown in Fig. 1, the hybrid vehicle-mounted energy harvester includes two independent energy harvesting structures: a flutter piezoelectric energy harvester (FPEH) and an electromagnetic vibration energy harvester (EVEH). The flutter piezoelectric energy harvesting structure consists of a piezoelectric beam with a tip magnet, a rigid airfoil with a hinged connection to the free end of the beam. To prevent the piezoelectric patch from being damaged by excessive deformation when the wind speed is too high, the substrate is designed as a two-stage stepped beam with different thicknesses. The electromagnetic vibration energy harvester is installed in the front of the leading edge of the airfoil. The airfoil will withstand the

effects of aerodynamic lift and aerodynamic moment under the action of airflow. When the frequencies of torsion and bending modes coalesce with each other, the flutter phenomenon occurs. Then piezoelectric cantilever oscillated in a limit cycle above a critical wind speed, and generate an AC voltage on the upper and lower surfaces of the piezoelectric patch. The vibration of the magnet A will drive the vibration of the magnets B in the coil, thereby generating alternating currents. This hybrid energy harvester can also withstand vibration in two directions for energy harvesting. Magnetic coupling between magnets A and B can achieve broadband harvesting from base vibrations, reduce the cut-in wind speed, and increase the energy harvesting effect [31], [40].

A. PIEZO-AEROELASTIC VIBRATION MODEL

To obtain the equations of motion, we use Hamilton's variational principle which states [43]

$$\int_{t_1}^{t_2} [\delta\,(\text{T-U}) + \delta W]\, dt = 0 \tag{1}$$

where T is the kinetic energy of FPEH, U is the potential energy of FPEH and δW is the virtual work done by the external force. To simplify the analysis process, assumptions are made as follows:

1) Magnet A is regarded as a particle, and its moment of inertia is ignored;
2) The substrate and the piezoelectric patch are adhered well, without considering the influence of the adhesive on the piezoelectric beam;
3) The electric field of the piezoelectric ceramics is uniformly distributed in the thickness direction (z-axis direction).

Let $w(x,t)$ be the displacement of a point on the beam in the z-axis direction, and where x and t are the x-direction coordinates and time, respectively. Note $\dot{w}(x,t) = \frac{\partial w(x,t)}{\partial t}$, $w'(x,t) = \frac{\partial w(x,t)}{\partial x}$. The deflection angle of a particle with an abscissa x on the piezoelectric beam respect to the z-axis is approximately equal to $w'(x,t)$ [44]. The kinetic energy of FPEH mainly includes the kinetic energy of the piezoelectric patch, the substrate, the airfoil, and the magnet A:

$$\begin{aligned} T = {} & \frac{1}{2}\int_0^{L_p}\int_{A_{b1}}^{\rho_b} (\dot{w}(x,t))^2\, dAdx \\ & + \frac{1}{2}\int_{L_p}^{L_b}\int_{A_{b2}}^{\rho_b} (\dot{w}(x,t))^2\, dAdx \\ & + \frac{1}{2}\int_0^{L_p}\int_{A_p}^{\rho_p} (\dot{w}(x,t))^2\, dAdx + \frac{1}{2}m_{At}\,[\dot{w}(L_b,t)]^2 \\ & + \frac{1}{2}m_F\,[\dot{w}(L_b,t)]^2 + m_F b x_\alpha \dot{\alpha}\dot{w}(L_b,t) + \frac{1}{2}I_F\dot{\alpha}^2 \end{aligned} \tag{2}$$

where ρ_s and ρ_p are the density of the substrate and the piezoelectric patch, respectively. A_{b1}, A_{b2} and A_p are the cross-sectional area of the fixed and free ends of the substrate and the piezoelectric patch, respectively. L_p and L_b are the length of the piezoelectric patch and the substrate, respectively. m_{At} is the mass of magnet A. m_F, b and I_F are the mass, the semi chord length, and the mass moment of inertia of the airfoil, respectively. x_α is the static unbalance parameter which is the non-dimensional distance between the center of gravity of airfoil and the axis of rotation. a is the non-dimensional distance from the half-chord to the rotation axis of the airfoil. α(rad) is the pitching displacement of the airfoil.

The potential energy includes strain energy and electric potential energy of the substrate and the piezoelectric patch. By introducing the geometric nonlinear condition formulated as $S_1 = -zw''\left(1 + \frac{1}{2}w'^2\right)$ [45], where z is the distance from a point of the cantilever beam to the neutral layer and S_1 represent the axial strain. The potential energy of the piezoelectric energy harvesting structure can be expressed as

$$\begin{aligned} U = {} & \frac{1}{2}\int_0^{L_b}\int_{A_{b1}} E_b S_1^2 dAdx + \frac{1}{2}\int_0^{L_b}\int_{A_{b2}} E_b S_1^2 dAdx \\ & + \frac{1}{2}\int_0^{L_p}\int_{A_p} E_p S_1^2 dAdx - \frac{1}{2}\int_0^{L_p}\int_{A_p} \varepsilon_{33}^S \frac{V_1^2}{t_p^2} dAdx \\ & - \int_0^{L_p}\int_{A_p} S_1 e_{31}\frac{V_1}{t_p} dAdx \end{aligned} \tag{3}$$

where E_b and E_p are Young's modulus of the substrate and piezoelectric patch, respectively; ε_{33}^S and e_{31} are the dielectric constant and piezoelectric constant of the piezoelectric patch, respectively; V_1 is the output voltage of FPEH. The influence of the non-conservative forces can be captured by introducing the general virtual-work term:

$$\begin{aligned} \delta W = {} & -Q_L\delta w(L_b,t) + Q_M\delta\alpha + F_{BA-z}\delta w(L_b,t) + Q\delta V_1 \\ & - \int_0^L c_a w(x,t)\delta w(x,t)\, dx \end{aligned} \tag{4}$$

where Q_L and Q_M are the aerodynamic lift and its moment applied on the airfoil, respectively. F_{BA-z} is the effective magnetic force acting on the tip of the beam. Q is the total electric charge on the electrodes of the piezoelectric transducers. c_a is the mechanical damping coefficient. The aerodynamic lift and its moment applied on the airfoil can be calculated by [31]

$$Q_L = \rho U^2 b s C_L\left(\alpha_{eff}\right) \tag{5}$$

$$Q_M = \rho U^2 b^2 s\left(\frac{1}{2} + a\right) C_L\left(\alpha_{eff}\right) - \frac{1}{2}\pi\rho U b^3 s\dot{\alpha} \tag{6}$$

where U is the wind speed, $C_L\left(\alpha_{eff}\right)$ is the quasi-steady aerodynamic lift coefficient, α_{eff} is the effective angle of attack due to the instantaneous motion of the airfoil and it is given by [18], [19]:

$$C_L\left(\alpha_{eff}\right) = a_{oL}\alpha_{eff} - \Delta C_L\left(\alpha_{eff}\right) \tag{7}$$

$$\alpha_{eff} = \alpha + \frac{\dot{h}}{U} + \left(\frac{1}{2} - a\right) b\frac{\dot{\alpha}}{U} \tag{8}$$

where a_{oL} is the linear lift coefficient. For the quasi-steady stall model, the aerodynamic force has been evaluated using the cubic polynomial approximation or the piecewise linear function as mentioned in. In this work, the piecewise linear

function is employed to model the aerodynamic force considering the stall effect, as follows [29], [31], [46]

$$\frac{\partial \Delta C_L\left(\alpha_{eff}\right)}{\partial \alpha_{eff}} = \begin{cases} 0, & -\bar{\alpha}_1 \le \alpha_{eff} \le \bar{\alpha}_1 \\ 6.3228, & \bar{\alpha}_1 \le \alpha_{eff} \le \bar{\alpha}_2, -\bar{\alpha}_2 \le \alpha_{eff} \\ & \le -\bar{\alpha}_1 \\ 5.9, & \bar{\alpha}_2 \le \alpha_{eff}, \alpha_{eff} \le -\bar{\alpha}_2 \end{cases} \tag{9}$$

where $\Delta C_L\left(\alpha_{eff}\right)$ is the difference between linear and nonlinear components of the aerodynamic coefficient curve.

To describe the vibration of the cantilever, the following assumptions are made on the cantilever beam: the piezoelectric cantilever beam follows the Ray-leigh-Ritz principle and the deflection of each particle in the x-direction of the cantilever beam is considered to be the superposition of vibration displacement in each mode. Under low-frequency excitation, the true dynamic characteristics of the cantilever can be described by the dynamic model of the cantilever in the first-order mode [47]:

$$w(x,t) = \phi_1(x)\, h(t) \tag{10}$$

where $\phi_1(x)$ is the first-order bending mode shape function of the cantilever beam, and in this paper, the finite element method is used to obtain the mode shape function; $h(t)$ is the time mode coordinate corresponding to the vibration displacement function. Substituting the (5) into (2), (3), and (4), according to the Hamilton principle (the (1)), the elastic governing equation of FPEH can be obtained:

$$\begin{cases} M_1\ddot{h} + m_F b x_\alpha \phi_1(L_b)\,\ddot{\alpha} + 2\xi_1\sqrt{K_1 M_1}\dot{h} + K_1 h \\ +K_2 V_1 h^2 + K_5 h^5 + K_3 h^3 + \theta_p V_1 = F_{BA-z} - Q_L \\ \quad m_F b x_\alpha \phi_1(L_b)\,\ddot{h} + I_p\ddot{\alpha} = Q_M \\ \quad C_p\dot{V}_1 + \dfrac{V_1}{R_1} - \theta\dot{h} - K_2 h^2\dot{h} = 0 \end{cases} \tag{11}$$

where M_1 is the equivalent mass; ξ_1 is the mechanical damping ratio of FPEH; $K_1, K_3, K_5,$ *and* K_2 are the linear stiffness coefficient;θ_p is the electromechanical coupling coefficient; ξ_1 is the damping ratio; F_{BA-z} is the combined force of magnet B and magnet C on magnet A in the z-direction. Q_L *and* Q_M are the aerodynamic lift and its moment applied on the airfoil, respectively. C_p is the equivalent capacitance of the piezoelectric patch and R_1 is the load resistance of the FPEH. The calculation formulas of the above parameters are as follows:

$$M_1 = \int_0^{L_p} \rho_s A_{b1}\phi_1^2(x)\,dx + \int_{L_p}^{L_b} \rho_s A_{b2}\phi_1^2(x)\,dx + \int_0^{L_p} \rho_p A_p \phi_1^2(x)\,dx + m_{tip}\phi_1^2(L) \tag{12}$$

$$K_1 = \int_0^{L_p} I_{b1}E_b\phi_1''^2(x)\,dx + \int_0^{L_p} E_p I_p \phi_1''^2(x)\,dx + \int_{L_p}^{L} I_{b2}E_b\phi_1''^2(x)\,dx \tag{13}$$

$$K_2 = \frac{1}{4}\frac{\left(h_c^2 - h_b^2\right)W_b}{t_p} e_{31}\phi_1'^3\left(L_p\right) \tag{14}$$

$$K_3 = 2\int_0^{L_p} I_{b1}E_b\phi_1''^2(x)\,\phi_1'^2(x)\,dx + 2\int_0^{L_p} E_p I_p \phi_1''^2(x)\,\phi_1'^2(x)\,dx + 2\int_{L_p}^{L} I_{b2}E_b\phi_1''^2(x)\,\phi_1'^2(x)\,dx \tag{15}$$

$$K_5 = \frac{3}{4}\int_0^{L_p} I_{b1}E_b\phi_1''^2(x)\,\phi_1'^4(x)\,dx + \frac{3}{4}\int_0^{L_p} E_p I_p \phi_1''^2(x)\,\phi_1'^4(x)\,dx + \frac{3}{4}\int_{L_p}^{L} I_{b2}E_b\phi_1''^2(x)\,\phi_1'^4(x)\,dx \tag{16}$$

$$C_p = \frac{W_b L_p \varepsilon_{33}^S}{t_p} \tag{17}$$

$$\theta_p = \frac{1}{2}\frac{\left(h_c^2 - h_b^2\right)W_b e_{31}}{t_p}\phi_1'\left(L_p\right) \tag{18}$$

where m_{tip} is the mass of the end of the cantilever beam, including the mass of magnet A, airfoil, and connectors. I_{b1}, I_{b2} *and* I_p are the area moments of inertia of the fixed and free ends of the substrate and the piezoelectric patch, respectively. t_p is the thickness of the piezoelectric patch. h_a is the thickness from the substrate boundary to the neutral layer and h_c is the thickness from the boundary of the piezoelectric layer to the neutral layer. And $h_b = h_c - t_p$.

B. MAGNETIC OSCILLATOR VIBRATION MODEL

The conversion of electromagnetic energy is based on Faraday's law. During the vibration process, the magnetic vibrator B is subjected to spring elastic force, inertial force, the magnetic force between the magnets A and B, and electromagnetic coupling force between the magnet B and the induction coil. The current in the coil complies with Kirchhoff's law. Assume that the vibration of magnet A has a small effect on the current in the coil and can be ignored. The electromechanical coupling equation of the EVEH can be expressed as

$$\begin{cases} M_2\ddot{u}_2 + C_2\dot{u}_2 + K_e u_2 + \theta_e I_2 = F_{AB-x} \\ \theta_e\dot{u}_2 - L_c\dot{I}_2 - (R_2 + R_C)\,I_2 = 0 \end{cases} \tag{19}$$

where M_2 is the mass of magnets B, θ_e is the electromagnetic coupling coefficient, u_2 is the displacement of the magnet B, K_e is the spring stiffness of the electromagnetic vibrator, C_2 is the mechanical damping coefficient of the EVEH, R_2 is the load resistance of the EVEH, I_2 is the current flowing through the resistor R_2, L_c is the coil inductance, R_c is the coil resistance value and u_2 is the vibration displacement of magnet B and F_{AB-x} represents the component of the repulsive force of magnet A to magnet B in the x-direction. The parameters' derivation process and calculation formulas can refer to the literature [40].

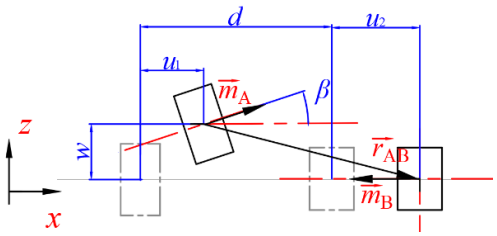

FIGURE 2. Geometric diagram of the relative position of endmost magnets.

C. COUPLING MAGNETIC FORCE AND SYSTEM MODEL

The magnetic moment vectors $\vec{m}_A$ and $\vec{m}_B$ are related to the volume of magnets. Denote the magnetic moments' value of the magnetic A and B be m_A and m_B and the direction is shown in Fig. 2. The magnetic moment vectors $\vec{m}_A$ and $\vec{m}_B$ can be expressed as

$$\vec{m}_A = m_A sin\beta \hat{e}_z + m_A cos\beta \hat{e}_x, \vec{m}_B = m_B \hat{e}_x \tag{20}$$

where β(rad) is the deviation angle of the end of the piezoelectric beam, $\hat{e}_z$ and $\hat{e}_x$ are the unit vector in the direction of x and z, respectively. The vector from the center of magnetic dipole A to the center of magnetic dipole B is:

$$\vec{r}_{AB} = w\hat{e}_z + (d + u_2 - u_1)\,\hat{e}_x \tag{21}$$

where u_1 is the displacement of magnet A in the x-direction during vibration, and $u_1 = \frac{1}{2}\int_0^{L_b} w' dx$ [43]. Considering the effect of the magnet A on magnet B, the magnetic potential energy of the magnetic B in this system is expressed as [48]:

$$U_{AB} = \frac{\mu_0 \vec{m}_A \vec{m}_B}{2\pi\,|\vec{r}_{AB}|^3} \tag{22}$$

where $\mu_0 = 4\pi \times 10\ \mathrm{Hm}^{-1}$, is the magnetic vacuum permeability. According to the relationship among the magnetic force, the potential energy and the geometrical position and vectors the magnetic force produced by magnetic A on magnetic B can be simply derived from the potential energy, as follows [48]

$$\vec{F}_{AB} = \frac{dU_{AB}}{d\vec{r}_{AB}} = -\frac{3\mu_0 \vec{m}_A \vec{m}_B}{2\pi\,|\vec{r}_{AB}|^4}\hat{r}_{AB} = F_{AB-z}\hat{e}_z + F_{AB-x}\hat{e}_x \tag{23}$$

where $\hat{r}_{AB}$ is the unit vector of $\vec{r}_{AB}$.F_{AB-x} is the component of $\vec{F}_{AB}$ in the x-direction, and is the effective magnetic force when the magnet B vibrates. And the effective magnetic force of the magnet A in the z-direction F_{BA-z} can be obtained: $F_{BA-z} = -F_{AB-z}$.

The governing electromechanical dynamic equation of the hybrid system is obtained, as follow (24), shown at the bottom of the page.

Define the state vector $\{q_1,\ q_2, q_3, q_4, q_5, q_6, q_7, q_8\}^T = \{h,\ \alpha, \dot{h}, \dot{\alpha}, V_1, u_2, \dot{u}_2, I_2\}^T$, and rearranging (24) results in the following vector field governing equations (25), as shown at the bottom of the page, where $M_{2\times2}$, $C_{2\times2}$ and $K_{2\times2}$ are the matrices stand for structural mass, damping, and linear stiffness of the FPEH, respectively.

III. NUMERAL CALCULATIONS

In this paper, the substrate material of the piezoelectric beam is copper, and the piezoelectric material is PZT-5H. The polarization direction of the piezoelectric patch is along the z coordinate. Magnet A and B are ring magnets. d takes the initial value of 30mm. The initial resistance load of FPEH R_1 is 70kΩ and the resistance load of the EVEH

$$\begin{cases} M_1\ddot{h} + m_F b x_\alpha \phi_1(L_b)\,\ddot{\alpha} + 2\xi_1\sqrt{K_1 M_1}\dot{h} + K_1 h + K_2 V_1 h^2 + K_5 h^5 + K_3 h^3 + \theta_p V_1 = F_{BA-z} - Q_L \\ m_F b x_\alpha \phi_1(L_b)\,\ddot{h} + I_p\ddot{\alpha} = Q_M \\ C_p\dot{V}_1 + \dfrac{V_1}{R_1} - \theta_p\dot{h} - K_2 h^2\dot{h} = 0 \\ M_2\ddot{u}_2 + C_2\dot{u}_2 + K_e u_2 + \theta_e I_2 = F_{AB-x} \\ \theta_e\dot{u}_2 - L_c\dot{I}_2 - (R_1 + R_C)\,I_2 = 0 \end{cases} \tag{24}$$

$$\begin{Bmatrix} \dot{q}_1 \\ \dot{q}_2 \\ \dot{q}_3 \\ \dot{q}_4 \\ \dot{q}_5 \\ \dot{q}_6 \\ \dot{q}_7 \\ \dot{q}_8 \end{Bmatrix} = \begin{bmatrix} q_3 \\ q_4 \\ M^{-1}\left(-C\begin{Bmatrix} q_3 \\ q_4 \end{Bmatrix} - K\begin{Bmatrix} q_1 \\ q_2 \end{Bmatrix} - \begin{Bmatrix} K_3 \\ 0 \end{Bmatrix} q_1^3 - \begin{Bmatrix} K_5 \\ 0 \end{Bmatrix} q_1^5 - \begin{Bmatrix} K_2 \\ 0 \end{Bmatrix} q_1^2 q_5 + \begin{Bmatrix} \theta_p \\ 0 \end{Bmatrix} q_5\right) \\ -\dfrac{\theta_p}{C_p}q_3 - \dfrac{1}{C_p R_L}q_5 - \dfrac{K_2}{C_p}q_1^2 q_3 \\ \dot{q}_7 \\ -\dfrac{C_2}{M_2}q_7 - \dfrac{K_e}{M_2}q_6 - \dfrac{\theta_e}{M_2}q_8 \\ \dfrac{\theta_e}{L_c}q_7 - \dfrac{R_2 + R_C}{L_c}q_8 \end{bmatrix} + \begin{Bmatrix} 0 \\ 0 \\ M^{-1}\begin{Bmatrix} F_{BA-z} - Q_L \\ Q_M \end{Bmatrix} \\ 0 \\ 0 \\ \dfrac{F_{AB-x}}{M_2} \\ 0 \end{Bmatrix} \tag{25}$$

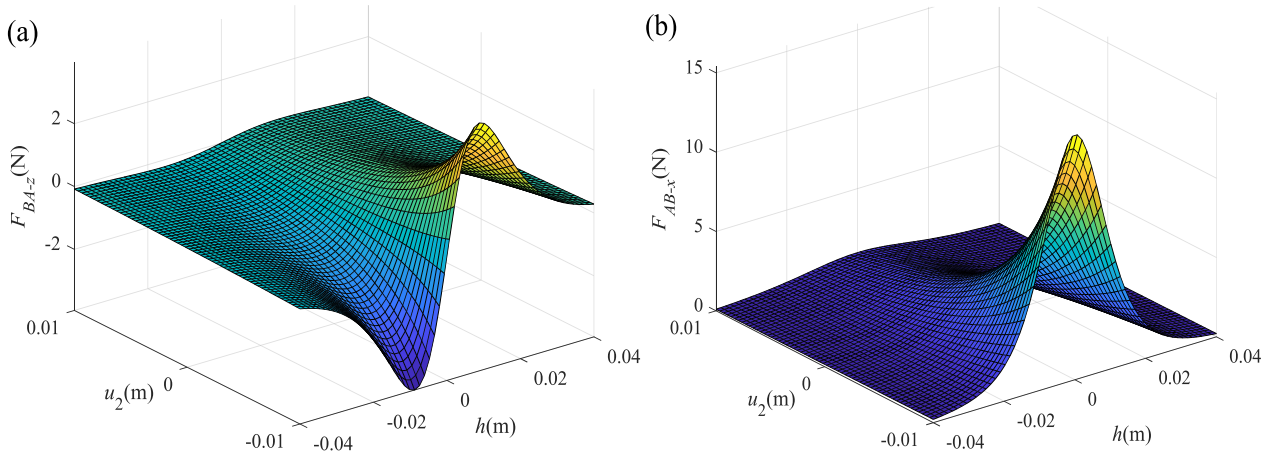

FIGURE 3. Effect of vibration displacements on magnetic forces (d = 30mm) (a)F_{BA-z}, (b)F_{AB-x}.

TABLE 1. Structural and material parameters.

Symbol	Parameters	Value
$L_p \times W_p \times t_p$	PZT length(mm)×width(mm) ×thickness(mm)	60×20×0.2
ρ_p, ρ_s	PZT and substrate density(kg/m^3)	7600, 8920
ε_{33}^S	PZT dielectric constant(nF/m)	25.6
e_{31}	PZT piezoelectric constant(C/m^2)	-16.6
E_p, E_b	Young's modulus of PZT and substrate layer (GPa)	60.6, 106
$L_b \times W_b \times t_{b1}$, $L_b \times W_b \times t_{b2}$	Substrate length(mm)×width(mm) ×thickness(mm)	60×25×0.6, 60×25×0.9
m_{tip}	End mass(g)	54.2
m_A, m_B	Magnetic moments(A/m)	1.17, 3.51
B_r	Residual magnetic flux density (T)	1.25
K_e	Spring stiffness (N/m)	166
θ_e	Electromechanical coupling coefficient of EVEH(T·m)	3.47
R_C	Coil resistance(Ω)	60.7
L_c	Coil inductance(H)	0.0143
m_F	Airfoil mass(g)	36
b	Airfoil semi chord(mm)	40
x_α	Airfoil static unbalance	0.4185
s	Airfoil span length(mm)	120
I_F	Airfoil mass moment of inertia(kg·mm^2)	9.684

R_2 is 120Ω. According to the research in the literature [40], to maximize the electromechanical coupling coefficient θ_e, the center height of the magnet B and the coil height are kept consistent. The initial damping ratios of FPEH and EVEH are both set as 0.02. The dimensions and material parameters of the hybrid system are shown in table 1.

According to the (23), when the initial magnet spacing d is 30mm, the changes of F_{BA-z} and F_{AB-x} with the vibration displacement h and u_2 are shown in Fig. 3. As can be seen from Fig. 3(a), F_{BA-z} increases with u_2 increasing, and has two extreme values in the positive and negative interval positions with the change of h. These two extreme values will become two potential energy traps when the piezoelectric vibrator vibrates. From Fig. 3(b) it can be seen that F_{AB-x} increases with u_2 increasing, and the maximum value is obtained when the displacement h is 0. When $h = 0$ and $u_2 = 0$, F_{AB-x} is not equal to 0, which means the initial position is not in a balanced state. To make the magnetic vibrator in a balanced state, the calculation formula of F_{AB-x} needs to be modified:

$$F_{AB-x} = F_{(AB-x)_1} - F_{(AB-x)_0} \tag{26}$$

where F_{AB-x} is the magnitude of the magnetic force after the correction, $F_{(AB-x)_1}$ is the magnitude of the magnetic force before the correction. $F_{(AB-x)_0}$ is the initial magnetic force of magnet A to magnet B when the system is at the initial position.

A. ANALYSIS OF OUTPUT CHARACTERISTICS

The output characteristics of the hybrid structure are shown in Fig. 4 to Fig. 6. Fig. 4 shows the amplitude attenuation curves below the cut-in wind speed. When the wind speed is 6m/s, the amplitudes of FPEH and EVEH, the output voltage and current will decay with time. And the outputs of voltage and current are relatively small. For classical flutter-based piezoelectric energy harvesting structures, with the wind speed increasing, the phase difference between the coupled bending and torsion modes will lead to the self-sustained positive work exerted by aerodynamic force-producing stable limit cycle oscillations [30], [49]. The coupling effect of the piezo-electromagnetic hybrid structure through the magnets will affect the vibration characteristics of the cantilever beam. The vibration characteristics of the piezoelectric vibrator and electromagnetic vibrator at wind speeds of 12 m/s and 18 m/s are shown in Fig. 5 and Fig. 6, respectively. It can be seen from Fig. 5(a) that when the wind speed is 12m/s, the displacement amplitudes of the piezoelectric vibrator reach 9.1mm. The vibration displacement of the electromagnetic vibrator does not vibrate around the initial position (the upper and lower amplitudes are not the same), and the absolute value of the lower amplitude is larger than

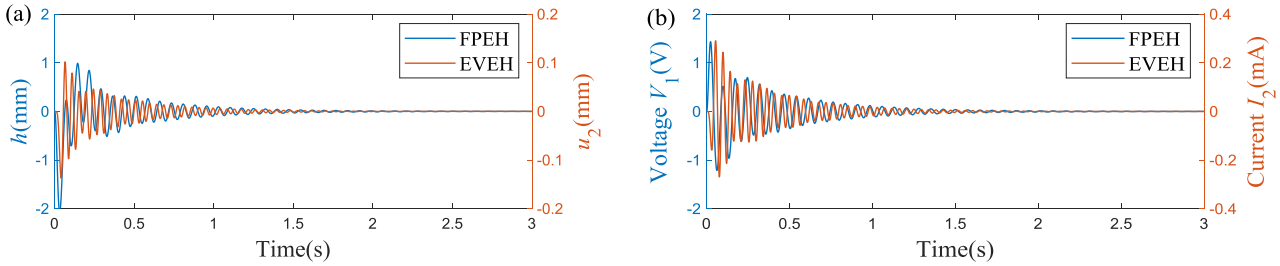

FIGURE 4. Time history curves (d = 30mm, U = 6m/s): (a) vibration displacements; (b)output voltage V_1 and current I_2.

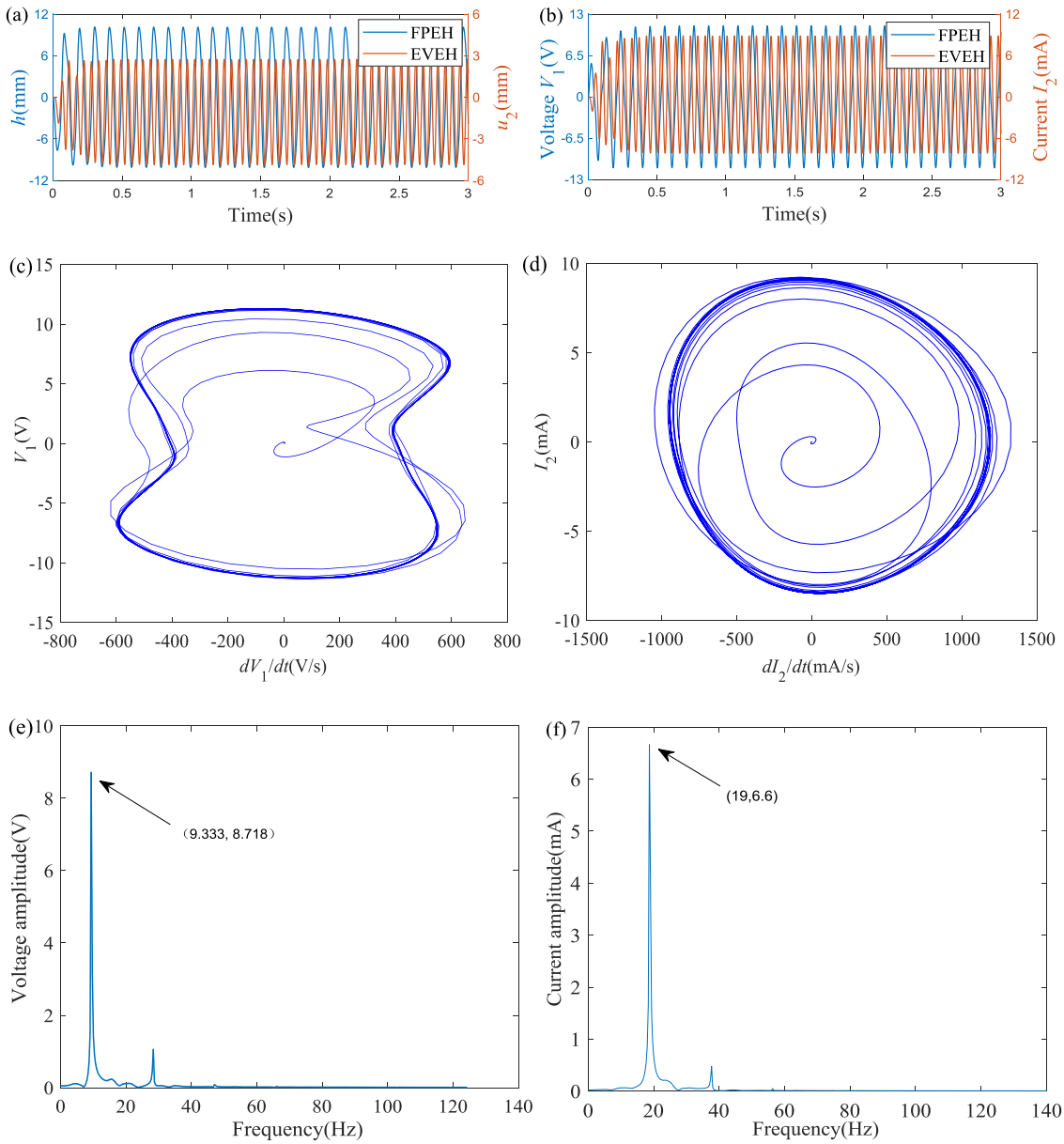

FIGURE 5. Time histories and phase plots of vibration displacement, output voltage and current amplitude-frequency characteristics (d = 30mm, U = 12m/s): (a) and (b) time histories; (c) and (d) phase plots; (e) and (f) amplitude-frequency characteristic curves of V_1 and I_2.

the upper amplitude. This is because when the piezoelectric vibrator starts to vibrate, the balance position has shifted to the left. It can be seen from Fig. 5(b) that the output voltage amplitude of the piezoelectric vibrator and current amplitude of the electromagnetic vibrator reached 10.6V and 8.5mA respectively.

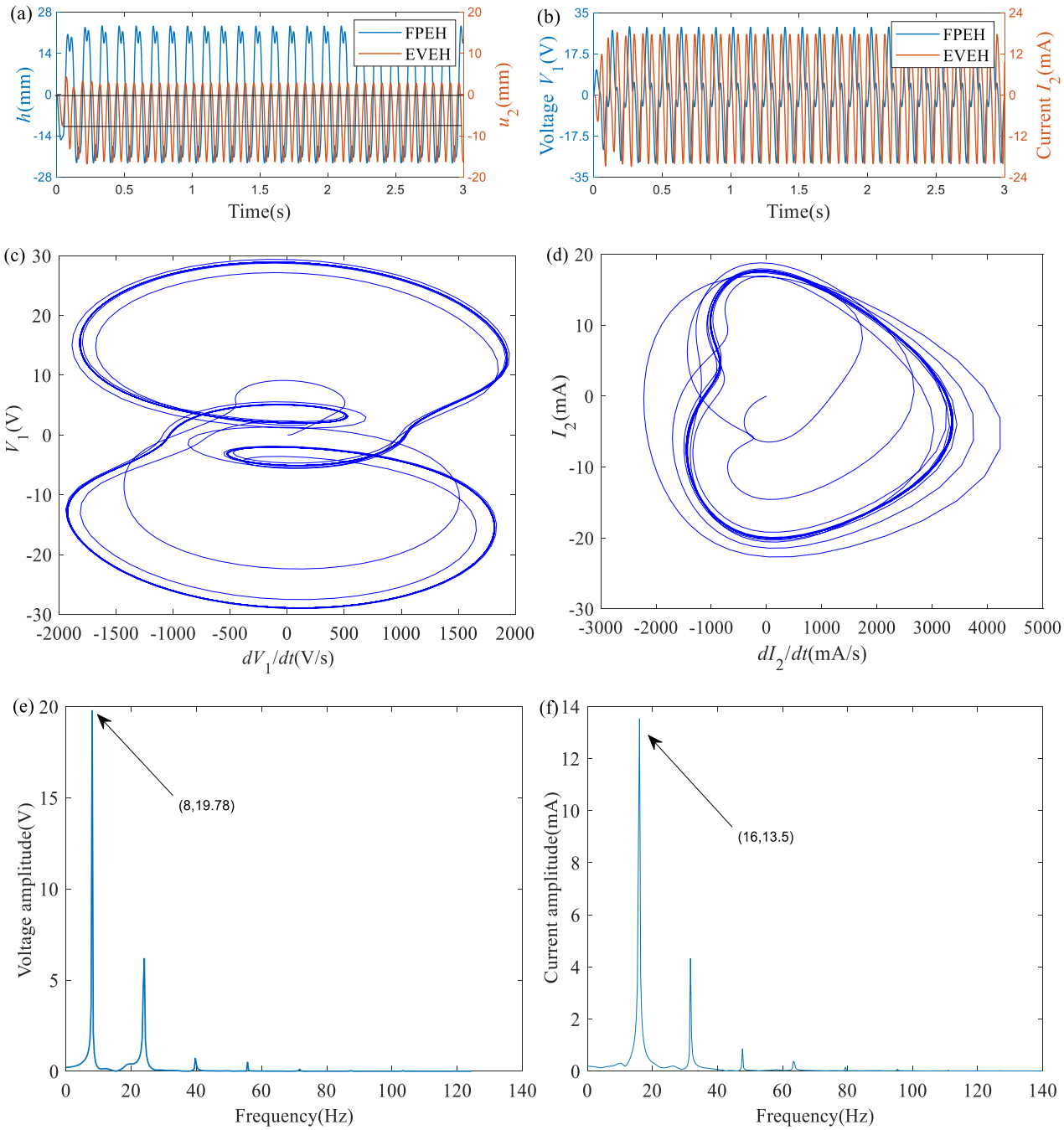

FIGURE 6. Time histories and phase plots of vibration displacement, output voltage and current amplitude-frequency characteristics (d = 30mm, U = 18m/s): (a) and (b) time histories; (c) and (d) phase plots; (e) and (f) amplitude-frequency characteristic curve of voltage and current.

From Fig. 5(c) and Fig. 5(d), it can be seen that the piezoelectric vibrator exhibits a bistable characteristic under the action of the magnetic force, which provides the basis for increasing the voltage output [37], [50]. The piezoelectric vibrator oscillates between two potential energy traps, and the electromagnetic vibrator exhibits an irregular nearly circular orbit. The amplitude-frequency characteristic curves of voltage and current are obtained by fast Fourier transform of voltage and current which are shown as Fig. 5(e) and Fig. 5(f). Both voltage power spectrum and current power spectrum exhibit multi-frequency characteristics, which is caused by the coupling effect between the two vibrators. The main frequency of the voltage is 9.33Hz, and the main frequency of the current is 19Hz which is exactly twice that of the voltage. This is because the vibration of the piezoelectric cantilever beam in one cycle exerts two symmetric dynamic magnetic forces on the electromagnetic vibrator.

As shown in Fig. 6(a) and Fig. 6(b), when the wind speed is 18m/s, the vibration displacement of the voltage vibrator reaches 29.3mm, the electromagnetic vibrator's vibration equilibrium position is -7.2mm, and the maximum displacement is -16.3mm. The peak values of voltage and current are

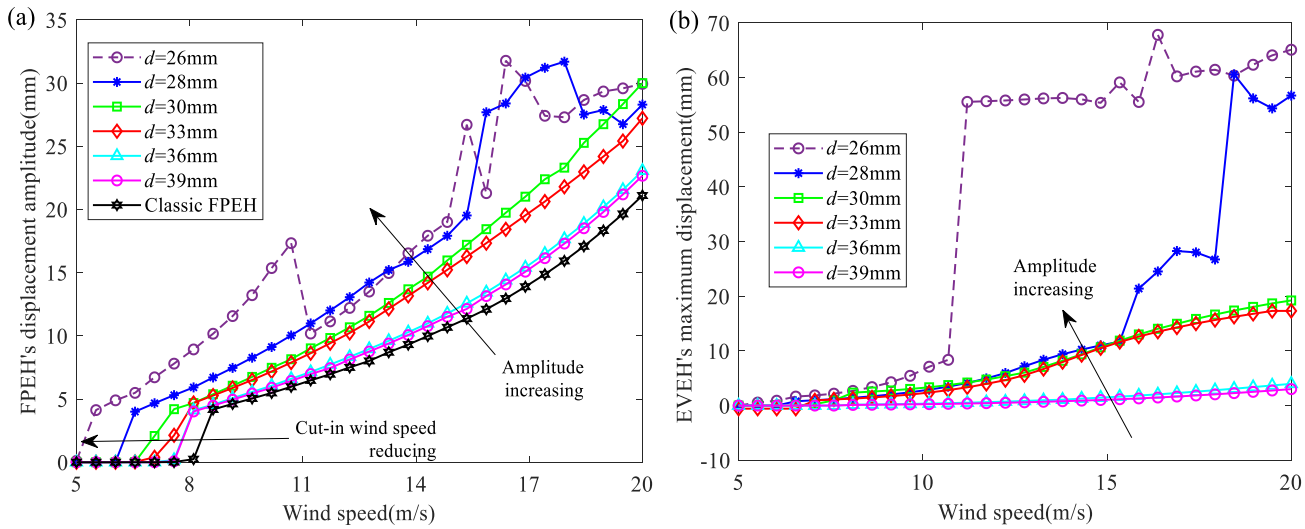

FIGURE 7. Displacement amplitude of the FPEH and EVEH changing with wind speed at different *d*: (a) FPEH; (b) EVEH.

29.2V and 23.5mA, respectively. It can be seen from Fig. 6(c) and Fig. 6(d) that the vibration of the piezoelectric vibrator is chaotic, and there is no stable vibration orbit. At the same time, the phase diagram of the current also appears chaotic, and the vibrating phase orbit exhibits an irregular shape. This is because the nonlinear phenomenon of the structure and the magnetic coupling nonlinear phenomenon are more obvious when the wind speed is higher so that chaos appears. From Fig. 6(e) and Fig. 6(f), it can be seen that the piezoelectric and electromagnetic vibrators still exhibit a multi-frequency phenomenon. The main frequencies of voltage and current are lower than the frequencies at 6m/s, which are 8Hz and 16Hz respectively.

B. INFLUENCE OF THE DISTANCE BETWEEN MAGNETS ON THE ENERGY HARVESTING EFFECT

To analyze the effect of the magnetic distance d on the output characteristics of the hybrid structure, six different magnetic distances are taken, and the displacement amplitude, voltage, and current amplitude, and frequency change characteristics are analyzed as shown in Fig.7 to Fig.10 and compared with the output characteristics of the classic flutter structure. It can be seen from Fig. 7 that when d is 30mm, 33mm, 36mm, and 39mm, respectively, the vibration displacement amplitude of the piezoelectric vibrator increases with the wind speed increasing above the cut-in wind speed and the vibration displacement amplitude is higher than that of the classic FPEH. The closer the magnet distance is, the more obvious the effect of amplitude increasing is. When the wind speed reaches 20m/s, the vibration displacement is 29.99mm, 27.21mm, 23.06mm, 22.67mm, respectively. The displacement amplitude of the classic FPEH is 21.1mm at 20m/s. When d is 30mm, the amplitude of the hybrid structure is increased by 0.42 times compared with the classic structure. The hybrid structure also has the effect of reducing the cut-in wind speed of the system, and the smaller the magnetic distance is, the more obvious the reduction effect is. When d is 30mm, the cut-in wind speed is 6.6m/s, which is 1.5m/s earlier than 8.1m/s of the classic FPEH. From Fig. 7(b), when d is taken as 30mm, 33mm, 36mm, and 39mm, the vibration displacement of the electromagnetic vibrator increases with the wind speed increasing. The smaller d is taken, the greater the vibration displacement is. When the d is 36mm and 39mm, the vibration displacement of the magnet B is significantly higher than that of d is taken 30mm and 33mm. When d is 39mm the vibration displacement of the magnetic vibrator is 3.088mm which is 0.84 times smaller than 19.23mm when d is 30mm. This is due to the magnetic force is too small when the larger magnetic distance is taken.

From Fig. 7(a) and Fig. 7(b), when d is 26mm and 28mm, the FPEH's displacement amplitude and the EVEH's maximum displacement both show irregular curves with the wind speed increasing. To analyze the reason, the time-domain curve of the electromagnetic vibrator's displacement when the wind speed is 12m/s and d takes 26mm is shown in Fig. 8. Under these conditions, the displacement u_2 of the electromagnetic vibrator fluctuates near the initial position of the electromagnetic vibrator before 0.3s. And after 0.3s, u_2 suddenly increases to 50mm-60mm (the negative sign in Fig. 8 only indicates the direction). This is mainly because the closer the magnets A and B are, the greater the magnetic force is, and the greater the amplitude is. The initial distance d between magnets B and the magnet A is only 26mm, which means that magnet B is already vibrating behind magnet A. When the position of the magnet B passes the position of the magnet A, the direction of the repulsive force of the magnet A to the magnet B will be reversed, resulting in a great displacement of the magnet B. In reality when the magnet B has such a large displacement, the spring will deform irreparably and the hybrid structure will be destroyed. For this

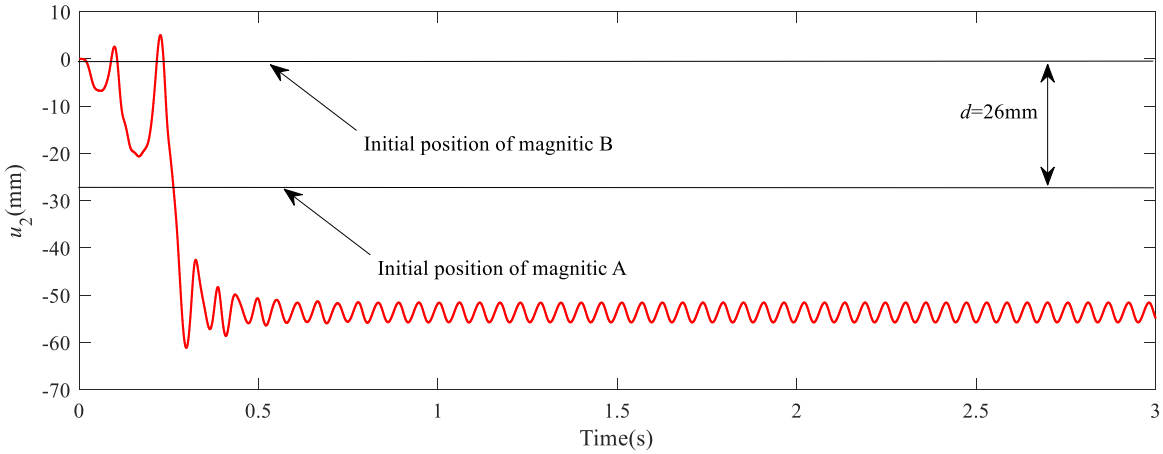

FIGURE 8. Time-domain curve of the electromagnetic vibrator's displacement at U = 12m/s and d = 26mm.

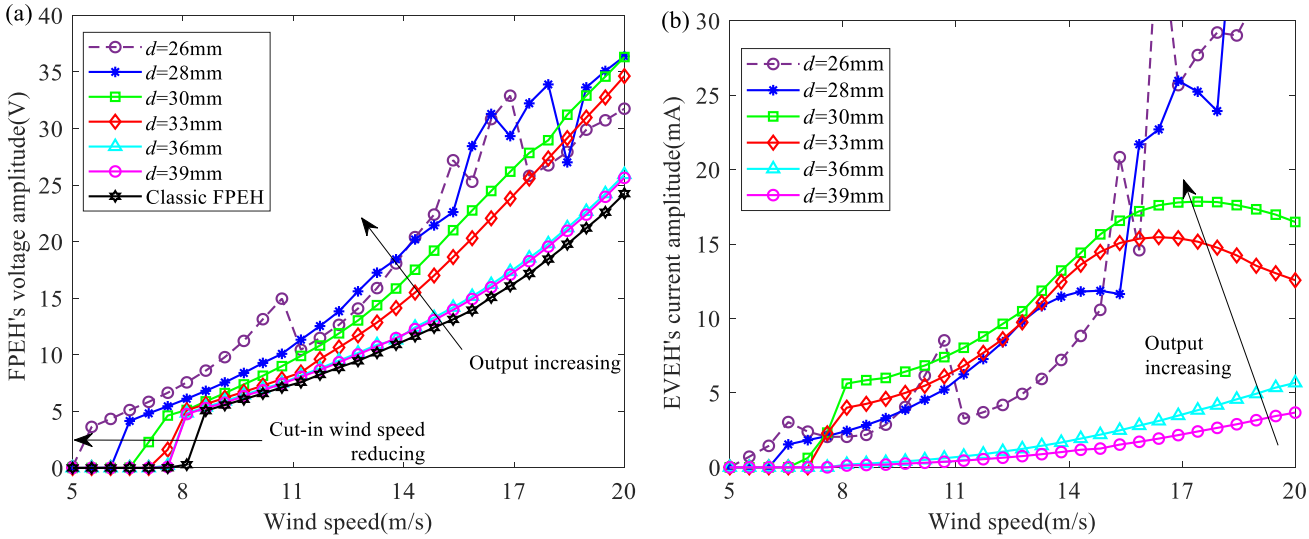

FIGURE 9. FPEH's voltage amplitude and EVEH's current amplitude changing with wind speed at different d: (a) voltage; (b) current.

reason, the vibration characteristics of the electromagnetic vibrator and the piezoelectric vibrator are irregular with the wind speed.

As shown in Fig. 9(a) and Fig. 9(b), both voltage and current increase with the wind speed increasing above the cut-in wind speed, and the smaller the magnetic distance, the better the energy harvesting effect. When d is 30mm and wind speed is 20m/s the voltage of FPEH is 36.32V, which is 0.50 times higher than that of classic FPEH's 24.25V, and the current of EVEH is 16.49mA which is 3.48 times higher than that of d is taken 39mm. Similarly, when d is 26mm and 28mm, the voltage and current output also show irregular changes. When d is taken as 30mm and 33mm respectively, the current curves show a downward trend after the peaks at 17m/s and 16m/s. In order to analyze the reason, the changes in the main frequency of voltage and current with wind speed are drawn as shown in Fig. 10. As the wind speed increases, the vibration frequency of the electromagnetic vibrator and the piezoelectric vibrator gradually decreases. As the distance between the magnets decreases, the vibration frequency of the piezoelectric vibrator and the electromagnetic vibrator also decrease.

Although the vibration displacement of the electromagnetic vibrator increases with the wind speed increasing, the vibration frequency decreases. The reduction of the vibration frequency leads to the reduction of the vibration speed and so that the output current decreases. Therefore, when d is 30mm, 33mm, and the wind speed is lower than 16m/s, the increase in amplitude leads to an increase in output current, and when the wind speed is higher than 16m/s, the decrease in frequency leads to a decrease in output current.

In these sets of data, for data other than d takes 28mm and 26mm, when d is 30mm, the amplitudes of FPEH's output voltage and EVEH's output current are the highest, and the cut-in wind speed is the lowest. When the magnet is closer, irregular changes in output characteristics are likely to occur, and even the large displacement of magnet B leads to damage to the hybrid structure.

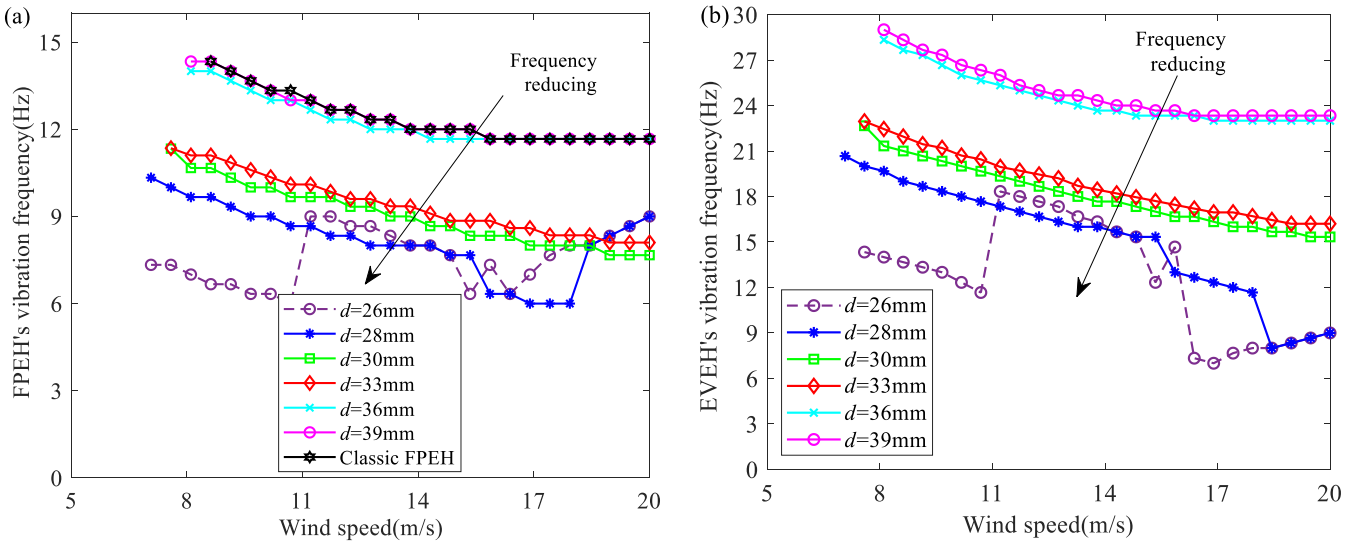

FIGURE 10. Frequency of FPEH and EVEH changing with wind speed at different d: (a) FPEH; (b) EVEH.

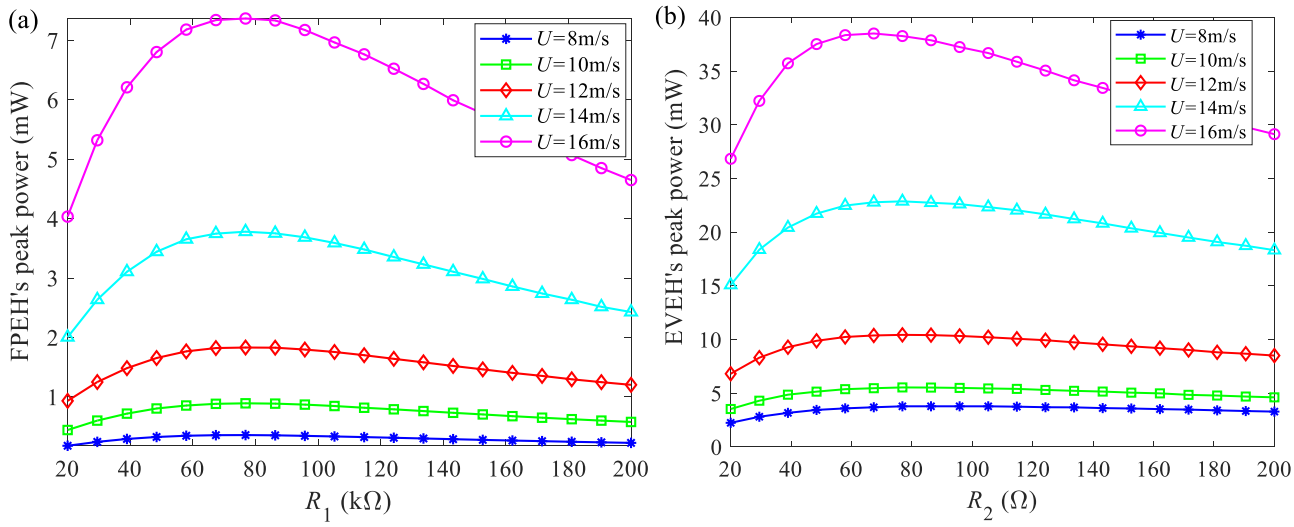

FIGURE 11. Output peak power changing with load resistances at different wind speeds: (a) FPEH, (b) EVEH.

C. INFLUENCE OF THE LOAD RESISTANCES ON THE ENERGY HARVESTING PERFORMANCE

The internal resistance of piezoelectric energy harvester is mainly capacitive internal resistance. The optimal matching load of FPEH is mainly related to the equivalent capacitance and vibration frequency. To discuss the effect of load resistance R_1 on the energy harvesting effect of FPEH, this article discusses the variation of the peak power of FPEH with the load resistance R_1 at five different wind speeds, as shown in Fig. 11(a). According to Fig. 11(a), when the wind speed is 8m/s,10m/s,12m/s,14m/s, and 16m/s respectively, the output peak power increases first and then decreases with the load resistance R_1 increasing, and the maximum value is obtained between 70kΩ-80kΩ. So the matching load of this FPEH is between 70kΩ-80kΩ. When the wind speed is low, the value of output power P_1 changes with the change of resistance R_1 is small. The internal resistance of EVEH is mainly related to the internal resistance of the coil. This paper analyzes the change of the peak power of EVEH with the load resistance R_2 under five different wind speeds as shown in Fig. 11(b). According to Fig. 11(b), when the wind speed is 8m/s,10m/s,12m/s,14m/s, and 16m/s respectively, the EVEH's output peak power increases first and then decreases with the load resistance R_2 increasing, and the maximum value is obtained between 60 Ω-70 Ω. Therefore the matching load of this EVEH is between 60Ω-70 Ω.

IV. EXPERIMENTS, RESULTS, AND DISCUSSION

A. EXPERIMENTAL SETUP

Fig.12 illustrates an experimental system for wind energy harvesting effect and the hybrid energy harvester prototype. A maximum uniform airflow velocity of 20 m/s can be achieved at the frequency converter (V8 4T 4R0GB, Shenzhen Veko Technology Electronics, Ltd., Shenzhen, China) of 50 Hz. The system consists of a cylindrical wind channel,

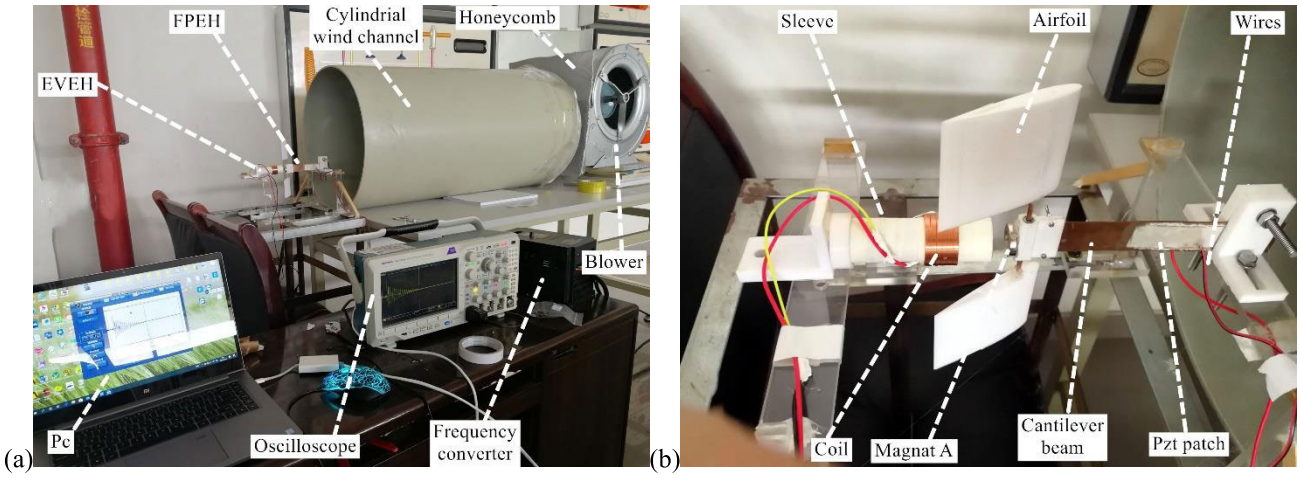

FIGURE 12. (a) Experimental devices; (b) hybrid energy harvester prototype.

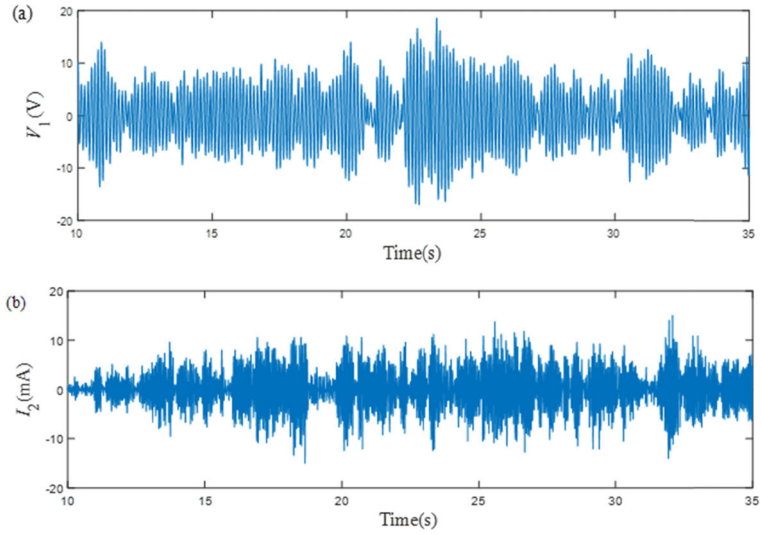

FIGURE 13. Experimental time histories of output voltage V_1 and current I_2 at 14m/s: (a) V_1; (b) I_2.

a super charging blower (DWF 3.15L, Shandong Kepuda Fan Co., Ltd., Dezhou, China), an energy harvester, an anemograph (AS-H3, Wuhan Zhongce Hongtu Measuring Instrument Co., Ltd, Wuhan, China), an oscilloscope (MDO 3014, Tektronix Inc., Beaverton, Oregon, USA). A honeycomb is used to form a steady airflow and decrease the disturbance. A PC and the digital storage oscilloscope can measure and record the output voltage and current, which across the external load resistances in real-time.

The stepped beam is made by pasting two copper patches of different lengths together. The substrate from 0 to L_p is formed by bonding two copper patches (0.6mm and 0.3mm) and that L_p–L_b segment has only one layer of 0.6mm copper patch. Adhesives between the piezoelectric patch and the copper plate and between the copper patches adopt conductive AB glue containing copper powder. After the completion of bonding, it can be used after 24h of holding pressure. The airfoil and connector are made by 3D printing and the material is PLA. Hinged columns are made of fine copper bars. The magnet of the electromagnetic vibrator is formed by the superposition of three ring magnets, and the connector between it and the spring is made by 3D printing. The electromagnetic vibrator is placed inside a sleeve, and the end of the sleeve is sealed to prevent wind from affecting the vibration of the magnet B. By installing a copper guidepost on the trajectory of magnet B, magnet B can only vibrate in one direction.

B. EXPERIMENTAL VALIDATION

From the optimal performance analysis results in Section III.B, i can be found that the energy harvesting characteristics are particularly better when thedistanceof magnes is 30mm. Therefore, the distanceof magnes is taken as 30mm. After the free deca vibration test [51] and preliminary simulation, the modal damping ratio of FPEH is set as $\xi_1 = 0.018$, and the modal damping ratio of EVEH is set as $\xi_2 = 0.038$. $_{R1}$ is set as70Ω and R2 is 60Ω. The other material parameters ar same as those in Table 1.

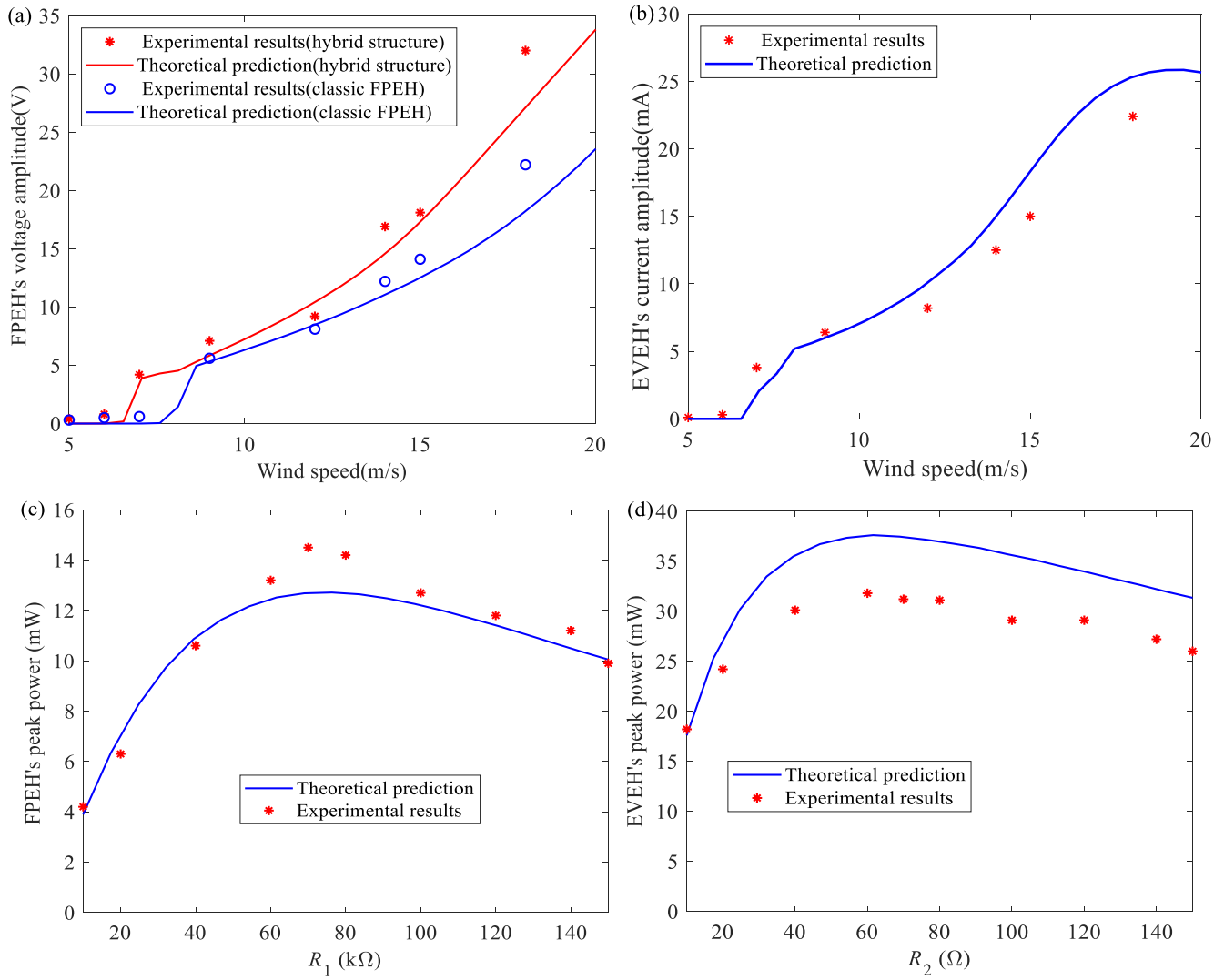

FIGURE 14. Comparisons of the output performance using the mathematical model and the experimental measurements: (a) and (b) the output voltage amplitude of FPEH and output current amplitude of EVEH changing with wind speed; (c) and (d) output peak power of FPEH and EVEH changing with load resistances at 18m/s.

Fig. 13 is the time-domain curve of voltage and current output when the wind speed is 14m/s. It can be seen from Fig. 13 that the output waveform in the time domain is confusing, which is caused by the fact that the test conditions cannot meet the ideal conditions of numerical simulation well. During the test, the wind supply device is relatively simple, it is hard to obtain a stable wind speed. The wind speed changes back and forth around a certain wind speed, so the amplitude of the time-domain voltage curve and current curve vary greatly. Due to it is difficult to compare the waveforms in the domain, this article only compares the amplitude of the output voltage and current. Fig. 14 is the comparison of the theoretical and experimental results of the output capability of the hybrid structure.

It can be seen from Fig. 14(a) that the experimental output voltage's amplitude change trends of the FPEH part of hybrid structure and classic FPEH with the wind speed are consistent with the theoretical predicted. After reaching the cut-in wind speed, the hybrid harvester's output voltage amplitude by the experimental test increases with the wind speed increasing. When the wind speed is 18m/s, the experimental result is 32.2V, which is 3.0V higher than the theoretically predicted value of 29.2V, and the error is 9.31%. At the same time, it can be seen that the output voltage is not 0 when the wind speed is 5m/s and 6m/s, which is due to the unstable wind speed output by the blower and the system vibration caused by the disturbance of the airflow. The variation trend of the classic FPEH's voltage amplitude with the wind speed is the same as that of the hybrid structure's FPEH, but it has higher cut-in wind speed and lower output. When the wind speed reaches 18m/s, the experimental voltage of the classic flutter structure is 22.2V. The experimental voltage of the hybrid structure is 45% higher than that of the classic FPEH. Achieved the purpose of reducing the cut-in wind speed and increasing the output.

From Fig. 14(b), it can be seen that the variation trend of the EVEH's output current amplitude with the wind speed by the experimental test is consistent with the theoretical prediction.

The output current amplitude by the experimental test is 22.4 mA at the wind speed of 18m/s, which is 2.8mA lower than the theoretically predicted value of 25.2mA. The error of the electromagnetic output current is mainly due to the axial magnetic force generated on the magnet B when the piezoelectric vibrator vibrates radial repulsive force, which will increase the friction between the electromagnetic vibrator and the guide column, thereby reducing the current output. Fig. 14(c) and 14(d) show the output peak power's change trend of FPEH and EVEH with load resistances changing at 18m/s. It can be seen from Fig. 14(c) that the FPEH's peak output power increases first and then decreases with the load resistance R_1 increasing, and obtains a maximum value of 14.5mW at 70kΩ, which is 1.82mW higher than the theoretically calculated 12.68mW. It can be seen from Fig. 14(d) that the EVEH's peak output power increases first and then decreases with the load resistance R_2 increasing, and obtains a maximum value of 31.8mW at 60Ω, which is 5.8 mW lower than the theoretical calculation of 37.6mW.

Accordingly, it is a powerful statement that the theoretical and experimental results are in good agreement. Although the experimental output voltage and current waveforms are not stable enough, the wind speed of the vehicle-mounted energy harvester in actual work cannot be stable. Therefore, this experiment also proved this vehicle-mounted energy harvester can achieve the purpose of powering low-power electronic devices (such as miniature accelerometers of 1mW level).

V. CONCLUSION

This work proposed a piezo-electromagnetic hybrid vehicle-mounted energy harvester that can recover the wind energy and vibration energy generated during driving. The coupled vibration mathematical model was established, and the output performances of the energy harvesting were analyzed and predicted. When the wind speed is 12m/s, the phase diagram exhibits bistable characteristics. When the wind speed reaches 18m/s, the structure of the phase diagram is chaotic. The effects of the different distances between magnets on the output were discussed. Results show that the energy-harvesting effect is the best when the distance between magnets is 30mm. At the same time, the numerical simulation proves that the hybrid structure is better than the classic FPEH. The combination of the two structures can play a role in reducing the cut-in wind speed. The experimental verification is carried out, and the theoretical prediction results are consistent with the experimental results, which verified the correctness of the theory. The optimal load of FPEH is 70kΩ, and the optimal load of EVEH is 60Ω. When the wind speed is 18m/s and R_1 is 70kΩ, the FPEH's peak output power is 14.5mW. And the EVEH's peak output power is 31.8mW at 18m/s when R_2 is 60Ω. The present work provides an effective theoretical and experimental foundation for the research of the energy harvesting and vibration control of the piezo-electromagnetic hybrid vehicle-mounted energy harvester.

REFERENCES

[1] M. A. A. Abdelkareem, L. Xu, M. K. A. Ali, A. Elagouz, J. Mi, S. Guo, Y. Liu, and L. Zuo, "Vibration energy harvesting in automotive suspension system: A detailed review," *Appl. Energy*, vol. 229, pp. 672–699, Nov. 2018, doi: 10.1016/j.apenergy.2018.08.030.

[2] H. Wang, A. Jasim, and X. Chen, "Energy harvesting technologies in roadway and bridge for different applications—A comprehensive review," *Appl. Energy*, vol. 212, pp. 1083–1094, Feb. 2018, doi: 10.1016/j.apenergy.2017.12.125.

[3] W. Zhang and X. Xi, "The innovation and development of Internet of vehicles," *China Commun.*, vol. 13, no. 5, pp. 122–127, May 2016, doi: 10.1109/CC.2016.7489980.

[4] X. Li, Z. Li, Q. Liu, and X. Shan, "Study on the critical wind speed of a resonant cavity piezoelectric energy harvester driven by driving wind pressure," *Micromachines-Basel*, vol. 10, no. 12, pp. 1–16, Dec. 2019, doi: 10.3390/mi10120842.

[5] K. Pancharoen, D. Zhu, and S. P. Beeby, "Temperature dependence of a magnetically levitated electromagnetic vibration energy harvester," *Sens. Actuators A, Phys.*, vol. 256, pp. 1–11, Apr. 2017, doi: 10.1016/j.sna.2017.01.011.

[6] C. Wei and X. Jing, "A comprehensive review on vibration energy harvesting: Modelling and realization," *Renew. Sustain. Energy Rev.*, vol. 74, pp. 1–18, Jul. 2017, doi: 10.1016/j.rser.2017.01.073.

[7] Y. K. Tan and S. K. Panda, "A novel piezoelectric based wind energy harvester for low-power autonomous wind speed sensor," in *Proc. 33rd Annu. Conf. IEEE Ind. Electron. Soc. (IECON)*, Taipei, Taiwan, Nov. 2007, pp. 2175–2180.

[8] K. Itani, A. De Bernardinis, Z. Khatir, and A. Jammal, "Comparative analysis of two hybrid energy storage systems used in a two front wheel driven electric vehicle during extreme start-up and regenerative braking operations," *Energy Convers. Manage.*, vol. 144, pp. 69–87, Jul. 2017, doi: 10.1016/j.enconman.2017.04.036.

[9] Y. Su, K. Zhang, and Q. Gong, "Theoretical and experimental study of an electromagnetic vibration energy harvester," *Ferroelectrics*, vol. 551, no. 1, pp. 69–87, Oct. 2019, doi: 10.1080/00150193.2019.1658031.

[10] K. Zhang, Y. Su, J. Ding, and Z. Duan, "A low-frequency wideband vibration harvester based on piecewise linear system," *Appl. Phys. A, Solids Surf.*, vol. 125, no. 5, pp. 340:1–340:10, Apr. 2019, doi: 10.1007/s00339-019-2630-9.

[11] X. Shan, H. Tian, D. Chen, and T. Xie, "A curved panel energy harvester for aeroelastic vibration," *Appl. Energy*, vol. 249, pp. 58–66, Sep. 2019, doi: 10.1016/j.apenergy.2019.04.153.

[12] J. Wang, L. Tang, L. Zhao, and Z. Zhang, "Efficiency investigation on energy harvesting from airflows in HVAC system based on galloping of isosceles triangle sectioned bluff bodies," *Energy*, vol. 172, pp. 1066–1078, Apr. 2019, doi: 10.1016/j.energy.2019.02.002.

[13] S. Zhou and J. Wang, "Dual serial vortex-induced energy harvesting system for enhanced energy harvesting," *AIP Adv.*, vol. 8, no. 7, pp. 075221:1–075221:10, Jul. 2018, doi: 10.1063/1.5038884.

[14] R. Usharani, G. Uma, and M. Umapathy, "Design of high output broadband piezoelectric energy harvester with double tapered cavity beam," *Int. J. Precis. Eng. Manuf.-Green Technol.*, vol. 3, no. 4, pp. 343–351, Oct. 2016, doi: 10.1007/s40684-016-0043-1.

[15] A. Bibo and M. F. Daqaq, "On the optimal performance and universal design curves of galloping energy harvesters," *Appl. Phys. Lett.*, vol. 104, no. 2, pp. 23901:1–23901:15, Jan. 2014, doi: 10.1063/1.4861599.

[16] U. Javed, H. L. Dai, and A. Abdelkefi, "Nonlinear dynamics and comparative analysis of hybrid piezoelectric-inductive energy harvesters subjected to galloping vibrations," *Eur. Phys. J. Special Topics*, vol. 224, nos. 14–15, pp. 2929–2948, Nov. 2015, doi: 10.1140/epjst/e2015-02599-y.

[17] A. Abdelkefi, J. M. Scanlon, E. McDowell, and M. R. Hajj, "Performance enhancement of piezoelectric energy harvesters from wake galloping," *Appl. Phys. Lett.*, vol. 103, no. 3, pp. 33903:1–33903:5, Jan. 2013, doi: 10.1063/1.4816075.

[18] M. Bryant and E. Garcia, "Modeling and testing of a novel aeroelastic flutter energy harvester," *J. Vibrat. Acoust.*, vol. 133, no. 1, pp. 11010–11011, Feb. 2011, doi: 10.1115/1.4002788.

[19] A. Abdelkefi, A. H. Nayfeh, and M. R. Hajj, "Modeling and analysis of piezoaeroelastic energy harvesters," *Nonlinear Dyn.*, vol. 67, no. 2, pp. 925–939, Jan. 2012, doi: 10.1007/s11071-011-0035-1.

[20] S.-D. Kwon, "A T-shaped piezoelectric cantilever for fluid energy harvesting," *Appl. Phys. Lett.*, vol. 97, no. 16, Oct. 2010, Art. no. 164102, doi: 10.1063/1.3503609.

[21] M. Bryant, E. Wolff, and E. Garcia, "Parametric design study of an aeroelastic flutter energy harvester," *Proc. SPIE*, vol. 7977, pp. 79770(S):1–79770(S):11, Jan. 2011, doi: 10.1117/12.880487.

[22] R. Naseer, H. L. Dai, A. Abdelkefi, and L. Wang, "Piezomagnetoelastic energy harvesting from vortex-induced vibrations using monostable characteristics," *Appl. Energy*, vol. 203, pp. 142–153, Oct. 2017, doi: 10.1016/j.apenergy.2017.06.018.

[23] B. H. Huynh and T. Tjahjowidodo, "Experimental chaotic quantification in bistable vortex induced vibration systems," *Mech. Syst. Signal Process.*, vol. 85, pp. 1005–1019, Feb. 2017, doi: 10.1016/j.ymssp.2016.09.025.

[24] C. Hou, X. Shan, L. Zhang, R. Song, and Z. Yang, "Design and modeling of a magnetic-coupling monostable piezoelectric energy harvester under vortex-induced vibration," *IEEE Access*, vol. 8, pp. 108913–108927, May 2020, doi: 10.1109/ACCESS.2020.3000526.

[25] L. A. Weinstein, M. R. Cacan, P. M. So, and P. K. Wright, "Vortex shedding induced energy harvesting from piezoelectric materials in heating, ventilation and air conditioning flows," *Smart Mater. Struct.*, vol. 21, no. 4, pp. 45003:1-45003:10, Jan. 2012, doi: 10.1088/0964-1726/21/4/045003.

[26] Y. Hu, B. Yang, X. Chen, X. Wang, and J. Liu, "Modeling and experimental study of a piezoelectric energy harvester from vortex shedding-induced vibration," *Energy Convers. Manage.*, vol. 162, pp. 145–158, Apr. 2018, doi: 10.1016/j.enconman.2018.02.026.

[27] R. Song, X. Shan, X. Yang, T. Xu, X. Yang, and T. Xie, "Current status of research on fluid energy capture technology based on piezoelectric energy harvesters," *Vib. Shock*, vol. 38, no. 17, pp. 244–250, Apr. 2019, doi: 10.13465/j.cnki.jvs.2019.17.034.

[28] V. C. Sousa, M. M. de Anicézio, C. De Marqui, Jr., and A. Erturk, "Enhanced aeroelastic energy harvesting by exploiting combined nonlinearities: Theory and experiment," *Smart Mater. Struct.*, vol. 20, no. 9, pp. 94007:1–94007:8, Aug. 2011, doi: 10.1088/0964-1726/20/9/094007.

[29] Y. Wu, D. Li, J. Xiang, and A. Da Ronch, "Piezoaeroelastic energy harvesting based on an airfoil with double plunge degrees of freedom: Modeling and numerical analysis," *J. Fluids Struct.*, vol. 74, pp. 111–129, Oct. 2017, doi: 10.1016/j.jfluidstructs.2017.06.009.

[30] K. Li, Z. Yang, and S. Zhou, "Performance enhancement for a magnetic-coupled bi-stable flutter-based energy harvester," *Smart Mater. Struct.*, vol. 29, no. 8, pp. 1–31, May 2020, doi: 10.1088/1361-665X/ab9238.

[31] K. Li, Z. Yang, Y. Gu, S. He, and S. Zhou, "Nonlinear magnetic-coupled flutter-based aeroelastic energy harvester: Modeling, simulation and experimental verification," *Smart Mater. Struct.*, vol. 28, no. 1, pp. 15020:1–15020:15, Nov. 2019, doi: 10.1088/1361-665X/aaede3.

[32] I. L. Cassidy, J. T. Scruggs, S. Behrens, and H. P. Gavin, "Design and experimental characterization of an electromagnetic transducer for large-scale vibratory energy harvesting applications," *J. Intell. Mater. Syst. Struct.*, vol. 22, no. 17, pp. 2009–2024, Nov. 2011, doi: 10.1177/1045389X11421824.

[33] D. Shi, L. Chen, R. Wang, H. Jiang, and Y. Shen, "Design and experiment study of a semi-active energy-regenerative suspension system," *Smart Mater. Struct.*, vol. 24, no. 1, pp. 15001:1–15001:12, Nov. 2015, doi: 10.1088/0964-1726/24/1/015001.

[34] B. Wu, Y. Fang, and L. Deng, "Summary of energy collection application in vehicle tire pressure monitoring system," in *Proc. 4th Int. Conf. Autom., Control Robot. Eng. (CACRE)*, Shenzhen, China, 2019, pp. 1–9.

[35] S. Sadeqi, S. Arzanpour, and K. H. Hajikolaei, "Broadening the frequency bandwidth of a tire-embedded piezoelectric-based energy harvesting system using coupled linear resonating structure," *IEEE/ASME Trans. Mechatronics*, vol. 20, no. 5, pp. 2085–2094, Oct. 2015, doi: 10.1109/TMECH.2014.2362685.

[36] F. Khameneifar and S. Arzanpour, "Energy harvesting from pneumatic tires using piezoelectric transducers," in *Proc. Smart Mater., Adapt. Struct. Intell. Syst.*, vol. 1, Ellicott City, MD, USA, Jan. 2008, pp. 1–7.

[37] N. Tran, M. H. Ghayesh, and M. Arjomandi, "Ambient vibration energy harvesters: A review on nonlinear techniques for performance enhancement," *Int. J. Eng. Sci.*, vol. 127, pp. 162–185, Jun. 2018, doi: 10.1016/j.ijengsci.2018.02.003.

[38] S. Mahmoudi, N. Kacem, and N. Bouhaddi, "Enhancement of the performance of a hybrid nonlinear vibration energy harvester based on piezoelectric and electromagnetic transductions," *Smart Mater. Struct.*, vol. 23, no. 7, pp. 1–14, Jun. 2014, doi: 10.1088/0964-1726/23/7/075024.

[39] K. Itani, A. De Bernardinis, Z. Khatir, and A. Jammal, "Comparative analysis of two hybrid energy storage systems used in a two front wheel driven electric vehicle during extreme start-up and regenerative braking operations," *Energy Convers. Manage.*, vol. 144, pp. 69–87, Jul. 2017, doi: 10.1016/j.enconman.2017.04.036.

[40] Z. Xu, X. Shan, D. Chen, and T. Xie, "A novel tunable multi-frequency hybrid vibration energy harvester using piezoelectric and electromagnetic conversion mechanisms," *Appl. Sci.*, vol. 6, no. 1, pp. 1–16, Jan. 2016, doi: 10.3390/app6010010.

[41] Y. Tadesse, S. Zhang, and S. Priya, "Multimodal energy harvesting system: Piezoelectric and electromagnetic," *J. Intell. Mater. Syst. Struct.*, vol. 20, no. 5, pp. 625–632, Mar. 2009, doi: 10.1177/1045389X08099965.

[42] P. Li, S. Gao, and H. Cai, "Modeling and analysis of hybrid piezoelectric and electromagnetic energy harvesting from random vibrations," *Microsyst. Technol.*, vol. 21, no. 2, pp. 401–414, Dec. 2013, doi: 10.1007/s00542-013-2030-6.

[43] A. Bibo, G. Li, and M. F. Daqaq, "Electromechanical modeling and normal form analysis of an aeroelastic micro-power generator," *J. Intell. Mater. Syst. Struct.*, vol. 22, no. 6, pp. 577–592, Apr. 2011, doi: 10.1177/1045389X11400929.

[44] R. Song, X. Shan, F. Lv, and T. Xie, "A study of vortex-induced energy harvesting from water using PZT piezoelectric cantilever with cylindrical extension," *Ceram. Int.*, vol. 41, pp. S768–S773, Jul. 2015, doi: 10.1016/j.ceramint.2015.03.262.

[45] H. F. Tiersten, "On the derivation of the equation for the deflection of thin beams," *Math. Mech. Solids*, vol. 11, no. 2, pp. 176–180, Apr. 2006, doi: 10.1177/1081286504038590.

[46] D. M. Tang and E. H. Dowell, "Comments on the onera stall aerodynamic model and its impact on aeroelastic stability," *J. Fluids Struct.*, vol. 10, no. 4, pp. 353–366, May 1996, doi: 10.1006/jfls.1996.0023.

[47] S. Zhou, J. Cao, E. Alper, J. Lin, and X. Zhang, "Nonlinear model for piezoelectric energy harvester with magnetic coupling," *J. Xi'an Jiaotong Univ.*, vol. 48, no. 1, pp. 106–111, Oct. 2014, doi: 10.7652/xjtuxb201401018.

[48] S. Zhou, J. Cao, W. Wang, S. Liu, and J. Lin, "Modeling and experimental verification of doubly nonlinear magnet-coupled piezoelectric energy harvesting from ambient vibration," *Smart Mater. Struct.*, vol. 24, no. 5, pp. 550081-1–550081-14, Apr. 2015, doi: 10.1088/0964-1726/24/5/055008.

[49] A. Bibo and M. F. Daqaq, "Investigation of concurrent energy harvesting from ambient vibrations and wind using a single piezoelectric generator," *Appl. Phys. Lett.*, vol. 102, no. 24, Jun. 2013, Art. no. 243904, doi: 10.1063/1.4811408.

[50] A. Abdelkefi, A. H. Nayfeh, and M. R. Hajj, "Global nonlinear distributed-parameter model of parametrically excited piezoelectric energy harvesters," *Nonlinear Dyn.*, vol. 67, no. 2, pp. 1147–1160, Jan. 2012, doi: 10.1007/s11071-011-0059-6.

[51] R. Song, "Research on flow-induced vibration and power generation performance of cylindrical piezoelectric energy harvester," M.S. thesis, Mech. Eng., Harbin Inst. Technol., Harbin, China, 2016.

XIA LI was born in Shandong, China. She received the M.S. and Ph.D. degrees from the School of Mechatronics Engineering, Harbin Institute of Technology, in 2002 and 2007, respectively. She is currently an Associate Professor with the School of Mechanical and Power Engineering, Zhengzhou University. Her research interests include ultrasonic drive technology and application, ultrasonic molding technology of micro devices, application of piezoelectric energy harvesting technology in vehicles, and off-highway vehicle design and analysis.

ZHIYUAN LI was born in Henan, China, in 1995. He received the B.S. degree from the School of Mechanical and Power Engineering, Zhengzhou University, in 2018, where he is currently pursuing the M.S. degree. His main research interest includes energy harvesting.

CHENG BI was born in Henan, China, in 1996. He received the B.S. degree from the School of Vehicle Engineering, Kunming University of Science and Technology, in 2019. He is currently pursuing the M.S. degree with Zhengzhou University. His main research interest includes energy harvesting.

BENXUE LIU was born in Henan, China. He received the Ph.D. degree in mechanical design and automation from Chang'an University, in 2007. He is currently a Lecturer with the School of Mechanical and Power Engineering, Zhengzhou University. His research interests include structural fatigue life prediction and structural simulation optimization analysis, design and application research of special vehicles, and research and development of automated intelligent production lines for auto parts.

YUFENG SU (Member, IEEE) received the Ph.D. degree in microelectronics and solid state electronics from Shanghai Jiao Tong University, in 2006. He is currently a Professor with the School of Mechanical and Power Engineering, Zhengzhou University. His research interests include micro vibration energy harvesters and microactuators.